ELSEVIER

Journal of Nuclear Materials 288 (2001) 208–216

journal of nuclear materials

www.elsevier.nl/locate/jnucmat

Heavy-ion irradiation effects on structures and acid dissolution of pyrochlores

B.D. Begg *, N.J. Hess, W.J. Weber, R. Devanathan, J.P. Icenhower, S. Thevuthasan, B.P. McGrail

Pacific Northwest National Laboratory, Richland, WA 99352, USA

Received 22 March 2000; accepted 10 October 2000

Abstract

The temperature dependence of the critical dose for amorphization, using 0.6 MeV Bi^{+} ions, for $A_2Ti_2O_7$ pyrochlores, in which A = Y, Sm, Gd and Lu, exhibits no significant effect of A-site ion mass or size. The room temperature dose for amorphization was found to be ~0.18 dpa in each case. After irradiation with 2 MeV Au^{2+} ions glancing-incidence X-ray diffraction (XRD) revealed that each pyrochlore underwent an irradiation-induced structural transformation to fluorite in conjunction with amorphization. The effect of amorphization on the dissolution rates of fully dense pyrochlores, at 90°C and pH 2 (nitric acid) varied from a factor of 10 to 15 increase for $Gd_2Ti_2O_7$ to none for $Y_2Ti_2O_7$. Significant differences were observed in the A-site dissolution rates from the crystalline pyrochlores, indicating differences in the manner in which the A-site cations are incorporated into the pyrochlore structure. These indications were supported by Raman spectroscopy.

PACS: 61.10.Eq; 61.43.Er; 61.80.Jh; 61.82.Ms; 64.60.Cn; 81.05.Je

1. Introduction

Pyrochlore is one of a number of candidate materials proposed for the immobilization of actinide-rich wastes, and has recently been selected as a key component in the synroc-based pyrochlore-rich ceramics for the geological immobilization of excess weapons Pu. The pyrochlores under consideration typically exhibit $A_2B_2O_7$ stoichiometry, where actinides and lanthanides are incorporated on the A-site and either Ti or Zr occupy the B-site. One of the principal factors that will determine the suitability of a candidate wasteform is its aqueous durability. Given that actinide-bearing crystalline wasteforms will be subject to considerable α-recoil radiation damage leading to amorphization, it is important to understand the effect of the irradiation-induced crystalline-to-amorphous transformation on the aqueous durability of relevant pyrochlore compounds.

Irradiation-induced amorphization due to alpha decay has been previously studied in ^{244}Cm-doped $Gd_2Ti_2O_7$ [1–3]. The alpha-decay-induced amorphization process occurs heterogeneously at ambient temperature and results in 6.5% swelling, a decrease in hardness and elastic modulus, and a 20–50% increase in the ^{244}Cm and ^{240}Pu dissolution rates, respectively, at 90°C and pH ~ 6. The heterogeneous amorphization either occurs directly in the cascade of the ^{240}Pu alpha-recoil particle or from the overlapping of cascades, although the exact mechanism for amorphization has yet to be determined. Isochronal (12 h) annealing studies indicated that thermal recrystallization of the amorphous state in $Gd_2Ti_2O_7$ begins to occur at about 975 K [2]. Heavy ion-beam irradiation studies have also been used to study damage accumulation and amorphization

* Corresponding author. Present address: ANSTO, Materials Division, PMB 1, Menai, NSW 2234, Australia. Tel.: +61-2 9717 3747; fax: +61-2 9543 7179.

E-mail address: bruce.begg@ansto.gov.au (B.D. Begg).

0022-3115/01/$ - see front matter
PII: S0022-3115(00)00708-X

processes [4–6]. Raman spectroscopy results [4,5] show an exponential decrease in Raman intensity with dose leading to the complete loss of Raman intensity for the Gd–O and O–Gd–O modes in the amorphous state. Furthermore, Raman spectroscopy indicates that cation disordering, which would be consistent with the formation of a fluorite-like structure, occurs in conjunction with amorphization. The presence of fluorite in ion-beam irradiated $Gd_2Ti_2O_7$ has recently been confirmed by electron diffraction [6,7].

The present paper outlines the results of a more detailed study on the temperature dependence of amorphization in the $A_2Ti_2O_7$ system (A = Y, Sm, Gd, Lu), along with detailed characterization of the structural changes associated with amorphization, and the effects of amorphization on the dissolution rates of the A-site and Ti ions.

2. Experimental

All samples were prepared by a sol–gel route using an aqueous mix of titanium iso-propoxide and the appropriate rare-earth nitrate. These solutions were stir-dried and calcined at 700°C for 1 h in air. The calcine was then dried and wet ball-milled before being pressed into pellets and sintered in air at 1200°C for 12 h. The sintered pellets were subsequently powdered, dry and wet-milled, repressed and sintered in air at 1500°C for 30 h. The sintered pellets were then coated in boron nitride, encapsulated in glass and hot-isostatically pressed (HIP) at 1500°C for 2 h at 200 MPa in an argon atmosphere to produce fully dense samples.

The temperature dependence of irradiation-induced amorphization was studied over the temperature range 20–1000 K. The amorphization process was followed in situ by performing each irradiation in a transmission electron microscope using the HVEM-Tandem Facility at Argonne National Laboratory [8]. The TEM specimens were prepared by hand polishing followed by dimpling and ion milling with 5 keV Ar^+. The specimens were irradiated with 0.6 MeV Bi^+ ions and intermittently examined by selected area electron diffraction using a 300 keV electron beam, which was defocused during the actual ion-beam irradiation to eliminate any synergistic ionization effects. Beam heating of the sample during irradiation has been shown previously to be insignificant when good thermal contact exists between the sample the carbon film and the supporting grid. The critical ion fluence for complete amorphization at each temperature was determined by the loss of all crystalline diffraction maxima. The critical ion dose (dpa) was calculated using TRIM-97 and a displacement energy of 50 eV. The dpa was determined at a depth of 30 nm, which is the general region where amorphization should last occur.

Leach samples ($\sim$10 mm × 10 mm × 1 mm) were polished to a 0.5 μm diamond finish, and irradiated on both large faces with 2 MeV Au^{2+} ions to a fluence of 5 ions/nm^2 using the accelerator facilities within the Environmental Molecular Sciences Laboratory at PNNL [9]. Based on TRIM calculations, this fluence was more than three times the dose needed to amorphize the surface, and consequently would be expected to have produced amorphous surface layer depths of 360, 380, and 400 nm for A = Lu, Gd, and Y, respectively. Additional samples were irradiated to lower fluences of 0.3 and 0.75 ions/nm^2, which were expected to produce discontinuous and continuous buried amorphous layers, respectively. All these samples were examined by glancing-incidence X-ray diffraction (XRD).

Glancing-incidence XRD was carried out on a Philips PW3040/00 X'Pert MPD diffractometer using Cu Kα radiation. A variable slit was used to keep the irradiated area constant as 2θ varied, for each glancing angle. Integrated peak intensities were measured by fitting the diffraction peaks with pseudo-Voigt profiles, once the background had been subtracted with a cubic spline. Scanning electron microscopy (SEM) was performed on a LEO 982 Field Emission instrument operating at 20 kV. Compositional analyses were obtained using an Oxford ISIS energy dispersive spectrometer.

Raman spectra were measured on fully dense polished pyrochlore thin-sections, which were $<$2 μm thick, using a 1 mm spot size. Polarized Raman spectra were measured in backscattering geometry to minimize the substrate contribution using approximately 500 mW of 488.0 nm excitation from a CW argon ion laser. The Raman scattered light was scrambled prior to being focused on the entrance slit of a SPEX triple spectrometer. The exit slit was maintained at 75 μm and the scattered light was then dispersed onto a liquid nitrogen cooled charged coupled device Ge detector. The detector was calibrated using the Raman lines of a TiO_2 (anatase) standard. The Raman signal was collected for 60 s for all samples. The Raman spectra were analyzed using a commercially available software package, GRAMS.

The kinetics of pyrochlore dissolution were measured in a single pass flow-through (SPFT) apparatus. Dissolution rates were determined from two crystalline and two amorphous samples from each pyrochlore composition. Pyrochlore monoliths were placed in a basket-like sample holder that fits within a 60 ml Teflon reactor. The sample holders are grated, allowing solution access to all surfaces of the monoliths. The reactor assemblies were placed in a constant temperature oven at 90°C for experiment periods up to 37 days. Feed solutions were made up by adding $\sim$0.8 ml of 15.6 M nitric acid per litre deionized water, yielding pH values of 2.0 ± 0.1. Checks of pH values of the effluent solutions confirmed no deviations from the initial values. Infusion pumps maintained flow-through rates of 2–5 ml/day. At the

completion of the experiment the dissolution containers were acid-stripped to account for material that may have precipitated on the vessel walls and the leachates were filtered for colloids. Concentrations of elements in the sample effluent were measured by precise ICP-MS methods. In every case, we performed dilutions of the effluent to minimize solution matrix effects.

3. Results

X-ray diffraction of the HIP pyrochlores showed that they were single phase and pyrochlore structured. Scanning electron-microscopy confirmed the homogeneous single-phase nature of the samples, although very minor silicon impurities were occasionally present. The $Gd_2Ti_2O_7$ and $Y_2Ti_2O_7$ appeared to be fully dense whilst the $Lu_2Ti_2O_7$ exhibited a minor amount of open porosity. A sintered $Sm_2Ti_2O_7$ sample was also investigated as part of the study of the temperature dependence of amorphization. The results of the compositional analysis, along with the measured densities of the various pyrochlore samples are shown in Table 1.

3.1. Temperature dependence of amorphization

The temperature dependence of the critical dose to completely amorphize the samples by irradiation with 0.6 MeV Bi^+ ions is shown in Fig. 1. There is no significant effect of A-site ion mass or size on the temperature and dose dependence of amorphization. The amorphization dose exhibits a two-stage dependence on temperature, with a transition temperature between stages at about 500 K. Above 900 K, the dose for amorphization rises rapidly as the rate of recovery becomes similar to the rate of amorphization. This critical temperature for amorphization is close to the 975 K onset temperature measured for the thermal recrystallization of ^{244}Cm-doped $Gd_2Ti_2O_7$ [2]. At room temperature, the dose to completely amorphize all the samples is 0.18 ± 0.01 dpa, similar to the dose (0.155 dpa) required to amorphize ^{244}Cm-doped $Gd_2Ti_2O_7$ and the dose reported by others [10–12] for $Gd_2Ti_2O_7$ under irradiation with 0.6 MeV Ar^+, 1.0 MeV Kr^+ and 1.5 MeV Xe^+. This critical dose at room temperature helped define the irradiation conditions for the dissolution studies.

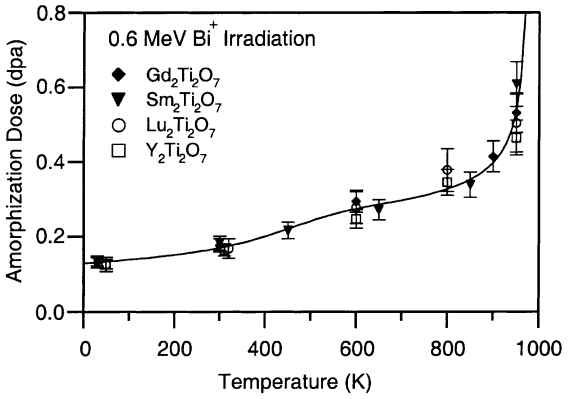

Fig. 1. Temperature dependence of the critical dose to amorphize each of the pyrochlore samples using 0.6 MeV Bi^+ ions, including a line of best fit.

The independence of pyrochlore amorphization on the A-site cation suggests that amorphization may occur via the breakup of the TiO_6 octahedral network, which is common to each of these pyrochlores.

3.2. Glancing-incidence XRD

3.2.1. TRIM calculations

Three separate samples from each pyrochlore composition were irradiated at room temperature with 2 MeV Au^{2+} ions to fluences of 0.3, 0.75, 3, and 5 ions/nm^2. TRIM calculations were used to predict the impact of these ion fluences on the pyrochlore structure. A sample TRIM calculation for $Gd_2Ti_2O_7$, using a displacement energy of 50 eV, showing the displacements-per-atom (dpa) as a function of depth for the various fluences is given in Fig. 2, along with the dpa (0.18 dpa) required to amorphize all three samples at room temperature. These calculations suggest that a 2 MeV Au^{2+} fluence of 0.3 ions/nm^2 is insufficient to form a continuous buried amorphous layer in $Gd_2Ti_2O_7$ and therefore would result in the formation of isolated amorphous regions due to the heterogeneous nature of the amorphization process, as observed in both ^{244}Cm-doped [1,2] and ion-irradiated [10] $Gd_2Ti_2O_7$. An ion fluence of 0.75 ions/nm^2 would be expected to amorphize a ~220 nm sub-surface layer beginning ~60 nm below the surface, whilst ion fluences of 3 and 5 ions/nm^2 would be ex-

Table 1
Summary of the microanalysis and density results for each of the pyrochlore samples

	$Gd_2Ti_2O_7$	$Y_2Ti_2O_7$	$Lu_2Ti_2O_7$	$Sm_2Ti_2O_7$
Composition[a]	$Gd_{2.02}Ti_{1.97}O_7$	$Y_{1.95}Ti_{2.04}O_7$	$Lu_{2.02}Ti_{1.98}O_7$	$Sm_{1.95}Ti_{2.04}O_7$
Density (g/cm^3)	6.54	4.94	7.24	–
% Theoretical density	99.6%	99.2%	98.3%	–

[a] Normalized to seven oxygen ions; cation abundances accurate to ±0.02 formula units.

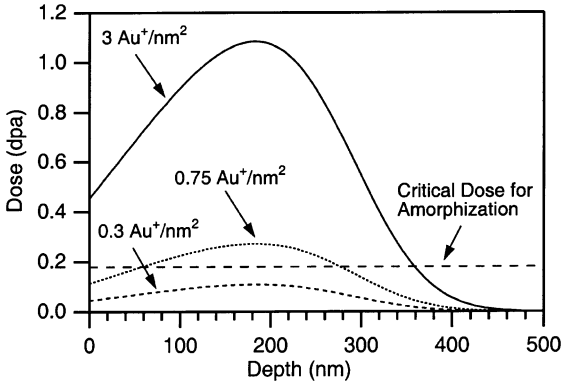

Fig. 2. TRIM-97 calculations showing predicted dose versus depth behaviour for three different fluences of 2 MeV Au^{2+} in $Gd_2Ti_2O_7$, including the critical amorphization dose.

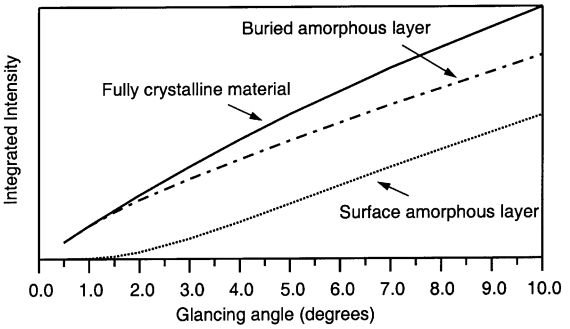

Fig. 3. Schematic representation of the effect of surface and buried amorphous layers on the integrated intensity versus glancing angle profile.

pected to fully amorphize the sample to a depth of 360 and 380 nm, respectively.

TRIM-based predictions of the effect of different 2 MeV Au^{2+} fluences on the structure of $Y_2Ti_2O_7$ and $Lu_2Ti_2O_7$ as compared to $Gd_2Ti_2O_7$ are shown in Table 2.

3.2.2. $Gd_2Ti_2O_7$

The structure of the 2 MeV Au^{2+}-irradiated pyrochlores was examined by glancing-incidence XRD. Measurements were taken using a range of glancing angles from 0.5° to 10° to characterize the structure as a function of depth. Integrated intensities of the major 222, 440 and 622 reflections were subsequently measured and plotted as a function of glancing angle. The profile of this plot was fitted with an amorphous and crystalline component to determine the depth of the amorphous layer.

The effect of both an amorphous surface layer and a buried amorphous layer, in an otherwise crystalline matrix, on the Bragg peak intensity versus glancing angle profile is schematically illustrated in Fig. 3.

Since an amorphous layer will not contribute to the intensity of the crystalline Bragg peaks, it may be considered purely as an absorption layer. The profile of the peak intensity versus glancing angle plot for a predominantly crystalline sample containing an amorphous surface layer will therefore be both displaced to higher glancing angles and attenuated due to the increased X-ray absorption, relative to a fully crystalline sample. The extent of the displacement will be proportional to the level of absorption from the amorphous surface layer and therefore its thickness. The principal factors that determine the extent of X-ray absorption are the X-ray absorption coefficients for the elements that constitute the sample, X-ray wavelength, sample density and the thickness of the amorphous layer. Since all these factors are known, apart from the thickness of the amorphous layer, the profile of this plot may be fitted with an absorption term, to account for the amorphous surface layer, and a crystalline term, which models both the absorption and diffracted intensity of the crystalline substrate, to determine the thickness of the amorphous surface layer. The mathematical equations used to describe these processes are well known [13]. In addition, the presence of an amorphous surface layer over a crystalline substrate will offset the Bragg peak positions to smaller 2θ values, since the crystalline surface is below the axis of diffraction.

In the case of the otherwise crystalline sample containing a buried amorphous layer, the integrated intensity versus glancing angle profile will initially follow that

Table 2
A summary of TRIM-97 calculations for four separate fluences of 2 MeV Au^{2+} ions on the different pyrochlore samples

2 MeV Au^{2+} (ions/nm^2)	$Gd_2Ti_2O_7$	$Y_2Ti_2O_7$	$Lu_2Ti_2O_7$
5	Amorphous layer 380 nm deep	Amorphous layer 400 nm deep	Amorphous layer 360 nm deep
3	Amorphous layer 360 nm deep	Amorphous layer 380 nm deep	Amorphous layer 340 nm deep
0.75	Buried amorphous layer from 55 to 275 nm	Buried amorphous layer from 100 to 290 nm	Buried amorphous layer from 45 to 260 nm
0.3	Damaged layer with isolated amorphous regions	Damaged layer with isolated amorphous regions	Damaged layer with isolated amorphous regions

of the fully crystalline sample until the X-rays begin to penetrate the buried amorphous layer. At this point the integrated intensity versus glancing angle profile will be attenuated, relative to the fully crystalline material, due to the X-ray absorption of the buried amorphous layer until, at some higher glancing angle, the X-rays are able to penetrate through the buried amorphous layer and diffract from the crystalline substrate.

Fig. 4 shows a selection of glancing-incidence diffraction patterns and the fit to the derived intensity versus glancing-angle data used to determine the thickness of the amorphous layer for $Gd_2Ti_2O_7$ irradiated with 3 Au^{2+}/nm^2. The thickness of the amorphous layer was determined to be $\sim 340 \pm 20$ nm, in excellent agreement with the $\sim$360 nm predicted by the TRIM calculation. The development of the broad amorphous background is clearly evident around the base of the 222 peak.

A summary of the glancing angle versus integrated intensity profile from the principal 222 peak for $Gd_2Ti_2O_7$ as a function of 2 MeV Au^{2+} fluence is shown in Fig. 5, along with the profile fits used to determine the thickness of the amorphous surface layers.

Fitting the integrated intensity versus glancing angle profile of the $Gd_2Ti_2O_7$ sample irradiated with 0.75 Au^{2+}/nm^2 indicated that it contained a $\sim$220 nm thick amorphous layer. Since the integrated intensity at the minimum 0.5° glancing angle was midway between that for the fully crystalline sample and that for the fully amorphous sample (3 Au^{2+}/nm^2), this amorphous layer must either be located just beneath the surface or else extends through to the surface in a discontinuous manner.

The $Gd_2Ti_2O_7$ sample irradiated with 0.3 Au^{2+}/nm^2 clearly contained a crystalline surface layer, as seen by the overlapping integrated intensity versus glancing angle profiles between it and the fully crystalline sample for

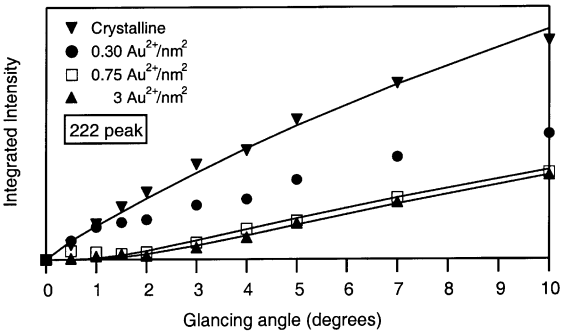

Fig. 5. Glancing-angle versus integrated 222 peak intensity data as a function of 2 MeV Au^{2+} fluence in $Gd_2Ti_2O_7$.

glancing angles up to 1.0°. Beyond 1.0°, the profile is displaced to higher glancing angles, with respect to the fully crystalline sample, which is consistent with the sample containing buried amorphous material. Further evidence for the crystalline surface layer and a buried amorphous layer is shown in Fig. 6, where the development of a broad peak around the sharp 222 pyrochlore reflection only occurred at glancing angles greater than 0.5°. In addition, certain peaks seen at glancing angles greater than 0.5° that correspond to the halved fluorite-subcell were also clearly asymmetric, as indicated in Fig. 6. This would indicate that the sample contained a sub-surface fluorite-structured phase, which is consistent with TEM results [10] that indicate $Gd_2Ti_2O_7$ undergoes a structural transformation from pyrochlore to fluorite in conjunction with amorphization and with Raman results [5] that show cation disordering at low fluences in $Gd_2Ti_2O_7$ irradiated with 3 MeV Ar^+ ions. The fluorite peaks were significantly broader than those from pyrochlore, which is consistent with the presence of strain and possibly particle-size

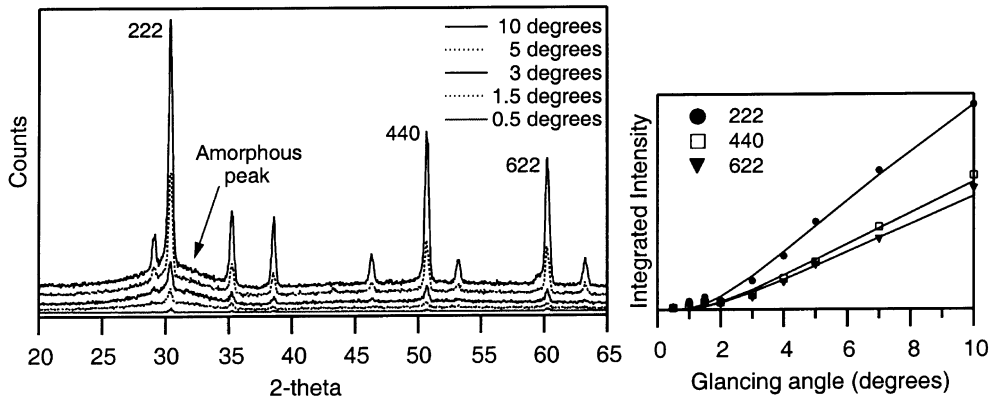

Fig. 4. Glancing-incidence X-ray diffraction patterns and the fitted integrated peak intensity data for the 222, 440 and 622 peaks used to determine the thickness of the amorphous layer in $Gd_2Ti_2O_7$ irradiated with 3 Au^{2+}/nm^2. The diffraction patterns have been offset for clarity, and are in the same order as they appear in the legend.

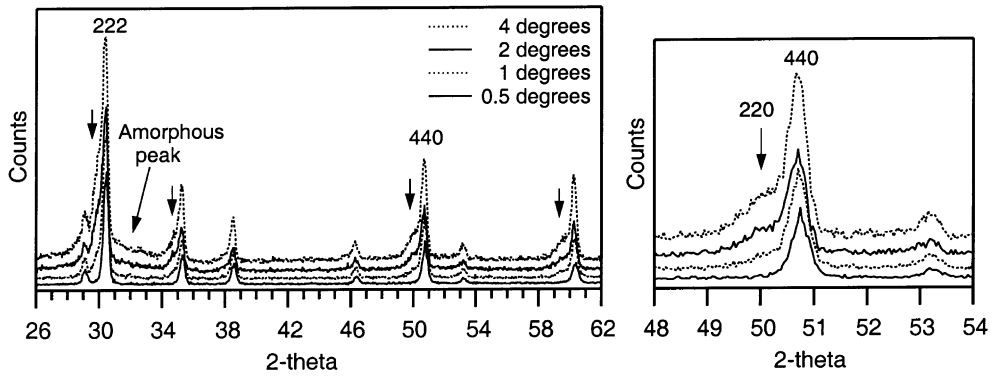

Fig. 6. Glancing-incidence X-ray diffraction patterns from $Gd_2Ti_2O_7$ irradiated with 0.3 Au^{2+}/nm^2 showing the positions of the fluorite reflections (↓) and the amorphous material. An expanded view around the 440 pyrochlore and 220 fluorite reflections is also shown. The diffraction patterns have been offset for clarity and are in the same order as they appear in the legend.

broadening in this irradiation-induced phase. Fitting the intensity versus glancing angle profile for the principal fluorite reflections indicated that it was present ~100 nm below the surface of the sample.

3.2.3. $Y_2Ti_2O_7$ and $Lu_2Ti_2O_7$

A summary of the glancing-incidence XRD results obtained from the $Y_2Ti_2O_7$ and $Lu_2Ti_2O_7$ pyrochlores is shown in Table 3. The $Gd_2Ti_2O_7$ findings discussed above have also been included for comparison.

The $Y_2Ti_2O_7$ and $Lu_2Ti_2O_7$ pyrochlore samples which had nominally received a dose of 0.75 Au^{2+}/nm^2, contained amorphous surface layers which were ~380 and ~300 nm thick, respectively. The thicknesses of these amorphous layers were slightly larger than predicted from the TRIM calculations, see Table 2. Each of the pyrochlore samples that had nominally received a dose of 0.3 Au^{2+}/nm^2 contained a fluorite-structured phase, providing further evidence that pyrochlore undergoes an irradiation induced structural transformation to fluorite prior to amorphization.

3.3. Raman studies

The crystalline $A_2Ti_2O_7$ pyrochlores (A = Gd, Lu and Y) were also examined by Raman spectroscopy to look for short-range structural differences. The Raman spectra from the $A_2Ti_2O_7$ pyrochlores are dominated by two intense bands at ~310 and ~512 cm^{-1} as shown in Fig. 7. These bands have been previously assigned to the O–A–O bending and A–O stretching modes, respectively [15]. The most notable difference in the Raman spectra between the various pyrochlores is the significant decrease in overall Raman intensity and increase in full-width-at-half-maximum (FWHM) intensity for the O–A–O bending and A–O stretching modes (also shown in Fig. 7) when Y is substituted into the A-site. The Raman shift, intensity and FWHM of the Ti–O stretching mode at approximately 450 cm^{-1} exhibited only minor variation between the various crystalline pyrochlore compositions.

The measurable width of a vibrational mode originates from an ensemble of different configurations in which the exact positions of atoms differ slightly, producing vibrational modes of nearly coincident frequency. Small distortions of the atomic positions affect the force constant of vibrational mode resulting in small shifts in vibrational frequency. Thus, the FWHM of a vibrational mode provides a measure of the level of localized short-range structural disorder in the material. Consequently, the considerable increase in FWHM of the A-site vibrational modes, combined with the notable

Table 3
A summary of glancing-incidence XRD results obtained from $Y_2Ti_2O_7$, $Lu_2Ti_2O_7$ and $Gd_2Ti_2O_7$ as a function of 2 MeV Au^{2+} fluence

Fluence (ions/nm^2)	$Y_2Ti_2O_7$	$Lu_2Ti_2O_7$	$Gd_2Ti_2O_7$
5	410 nm amorphous surface layer	320 nm amorphous surface layer	340 nm amorphous surface layer[a]
0.75	380 nm amorphous surface layer	300 nm amorphous surface layer	220 nm sub-surface amorphous layer
0.3	Sub-surface fluorite above a buried amorphous layer	Fluorite surface layer above a buried amorphous layer	Sub-surface fluorite above a buried amorphous layer

[a] Dose for $Gd_2Ti_2O_7$ was 3 ions/nm^2.

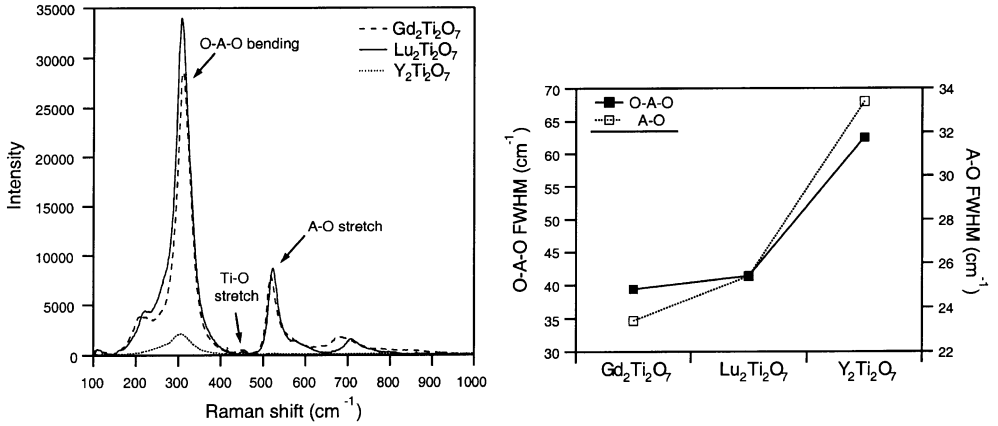

Fig. 7. Raman spectra from the crystalline $A_2Ti_2O_7$ pyrochlores (A = Gd, Lu and Y) are shown on the left, whilst the FWHM for the O–A–O bending and A–O stretching modes at ~310 and ~512 cm^{-1}, respectively, have been plotted on the right.

decrease in Raman intensity, observed for $Y_2Ti_2O_7$ suggests that the Y–O coordination environment is significantly more disordered than either the Gd or Lu coordination environments in $Gd_2Ti_2O_7$ and $Lu_2Ti_2O_7$, respectively. Thus despite their common crystal structures, the manner in which each of the titanate pyrochlores incorporates different A-site ions varies considerably between the different pyrochlores.

3.4. Dissolution studies

A comparison of the aqueous dissolution rates obtained from the fully dense amorphous and crystalline $Gd_2Ti_2O_7$ pyrochlore samples is shown in Fig. 8. The apparent initial (3–10 days) dissolution rates for Gd and Ti obtained from amorphous $Gd_2Ti_2O_7$ were approximately a factor of 15 higher than those measured from the crystalline samples. After 21 days, the dissolution rates for the amorphous samples were a factor of 10 and 2 higher for Gd and Ti, respectively. The significant drop in Ti dissolution rate with increasing time resulted from the precipitation of anatase, which was only found on the surfaces of the amorphous samples. There was no evidence for Gd precipitation, either on the sample surfaces or container walls. The Gd dissolution rates from the crystalline samples were found to be approximately a factor of 5 higher than the corresponding Ti dissolution rates, indicating incongruent dissolution. Characterization of the leached surfaces of the amorphous $Gd_2Ti_2O_7$ samples by glancing-incidence XRD indicated that the amorphous surface layer had been fully dissolved over the 21-day leach period, leaving behind a fluorite-structured surface layer. Based on TRIM calculations, fluorite would be expected to be present at depths between ~380–420 nm in the crystalline pyrochlore and its detection here at the surface of the leached pyrochlore has provided an objective measure of the dissolution depth in $Gd_2Ti_2O_7$ under our experimental conditions. The order of magnitude increase in dissolution rate for the amorphous material relative to the crystalline material is consistent with the 20- and 50-fold increase in Cm and Pu release, respectively, measured in amorphous ^{244}Cm-doped $Gd_2Ti_2O_7$ relative to the fully crystalline state at 90°C and pH 6 [1,14].

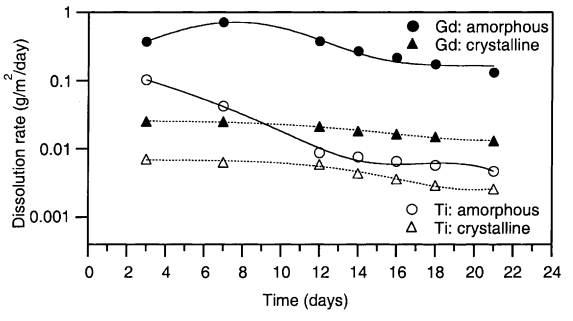

Fig. 8. A comparison of dissolution rates for crystalline and amorphous $Gd_2Ti_2O_7$ (g/m^2/day) leached at 90°C and pH 2 (nitric acid).

In contrast to the behaviour of Gd in $Gd_2Ti_2O_7$, the Y dissolution rates from the amorphous and crystalline $Y_2Ti_2O_7$ samples were identical as shown in Fig. 9. No apparent effect of amorphization was therefore evident in the Y dissolution rates. The initial Ti dissolution rate from the amorphous samples was however a factor of 6 higher than that obtained from the crystalline samples, which was about half the difference observed in $Gd_2Ti_2O_7$. At face value these results would suggest that the leaching behaviour of $Y_2Ti_2O_7$ was less susceptible to radiation damage than $Gd_2Ti_2O_7$. However, examination of the leached amorphous samples revealed that anatase was present on only one face of the leached

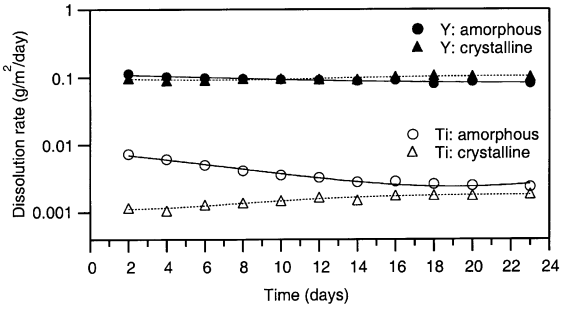

Fig. 9. A comparison of dissolution rates for crystalline and amorphous $Y_2Ti_2O_7$ (g/m^2/day) leached at 90°C and pH 2 (nitric acid).

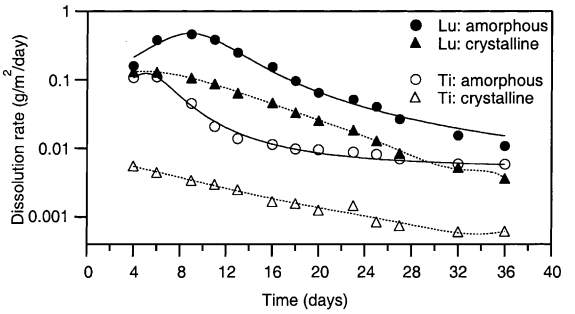

Fig. 10. A comparison of dissolution rates for crystalline and amorphous $Lu_2Ti_2O_7$ (g/m^2/day) leached at 90°C and pH 2 (nitric acid).

samples, which would imply that only one side of the samples had been amorphized and received twice the dose. No anatase was found on the surfaces of the leached crystalline samples. This might explain the factor of 2 difference observed between the initial Ti dissolution rate from the amorphous $Gd_2Ti_2O_7$ and $Y_2Ti_2O_7$ pyrochlores when compared to their crystalline counterparts, although it does not explain the failure to see any effect of amorphization in the Y dissolution rates. Significantly, the Y dissolution rates from crystalline $Y_2Ti_2O_7$ were at least a factor of 50 higher than those for Ti throughout the experiment, indicating that $Y_2Ti_2O_7$ is leaching incongruently. In fact, the Y dissolution rates from crystalline $Y_2Ti_2O_7$ were equivalent to the Gd dissolution rates from amorphous $Gd_2Ti_2O_7$. It is important to note that the final Ti dissolution rates from crystalline $Gd_2Ti_2O_7$ and $Y_2Ti_2O_7$ were identical. Glancing-incidence XRD of the leached amorphous surface of $Y_2Ti_2O_7$ revealed that the amorphous surface layer and the accompanying fluorite layer had been fully dissolved after the 23-day dissolution test. Therefore, despite their analogous crystal structures and equivalent Ti dissolution rates, the contrasting A-site dissolution behaviour of crystalline $Gd_2Ti_2O_7$ and $Y_2Ti_2O_7$ would suggest that Gd is bonded more strongly into the pyrochlore structure than Y. This is consistent with the Raman spectroscopy results that indicated that the Y–O coordination environment in crystalline $Y_2Ti_2O_7$ was significantly more disordered than the Gd–O environment in $Gd_2Ti_2O_7$ despite having similar Ti–O environments.

The initial Lu dissolution rates (after 4 days) from the amorphous and crystalline $Lu_2Ti_2O_7$ samples appear to be identical, as shown in Fig. 10; however this is an experimental artifact of the flow-through test and a better approximation is made after 9 days, when the Lu dissolution rate from the amorphous samples had peaked and the difference was a factor of ~5. At the completion of the 36-day dissolution period the dissolution rates from the amorphous sample were a factor of 3 higher than for the crystalline material. This would suggest that the Lu dissolution rate is relatively insensitive to amorphization. The initial Ti dissolution rate from the amorphous material was a factor of 20 higher than the crystalline material, though this decreased to a factor of 9 by the end of the experiment due to the precipitation of anatase. The amorphous layer had been fully dissolved at the end of the dissolution period. The Lu dissolution rates from the crystalline samples were just over a factor of 5 higher than Ti, at the end of the 36-day dissolution-period, which would suggest that the crystalline pyrochlore is leaching incongruently.

In summary, the dissolution behaviour of the amorphous pyrochlores at 90°C and pH 2 was found to be within a factor of 2 of each other over the common 21-day period. Consequently the significant differences observed between the amorphous and crystalline dissolution rates from the various pyrochlore compositions, reflect differences in the baseline behaviour of the crystalline pyrochlores, more than variations in the durability of the amorphous materials. The ratio of the Gd, Lu and Y 21-day dissolution rates from the three crystalline pyrochlores was 1:2:8, respectively, which must point to fundamental differences in the manner in which these A-site ions are incorporated into the pyrochlore structure. Notably the Ti dissolution rates from the crystalline pyrochlore compositions were all within a factor of 2 of each other. The significant discrepancies observed between the crystalline Gd or Lu and Y dissolution rates may possibly be attributed to the increased localized A-site disorder present in $Y_2Ti_2O_7$, when compared with either $Gd_2Ti_2O_7$ or $Lu_2Ti_2O_7$, as indicated by Raman spectroscopy.

4. Conclusions

No significant effect of A-site ion mass or size was seen in the temperature dependence of the critical dose for amorphization of the $A_2Ti_2O_7$ pyrochlores, for

A = Y, Sm, Gd and Lu. The room temperature dose for amorphization was found to be ~0.18 dpa. Each pyrochlore underwent an irradiation-induced structural transformation to fluorite in conjunction with amorphization. It has yet to be determined whether this transformation occurs prior to local amorphization or in parallel to amorphization processes. The thickness of the amorphous layers, determined by glancing-incidence XRD, was in good agreement with the values predicted by TRIM. The initial Gd and Ti dissolution rates from amorphous $Gd_2Ti_2O_7$ were a factor of 15 higher than from crystalline $Gd_2Ti_2O_7$. No effect of amorphization was evident in the Y dissolution rates, which were a factor of 10 higher than the Gd dissolution rates from crystalline $Gd_2Ti_2O_7$. The dissolution rate from crystalline $Lu_2Ti_2O_7$ was approximately equivalent to crystalline $Gd_2Ti_2O_7$. The final Lu dissolution rates from the amorphous pyrochlore were only a factor of 3 higher than from its crystalline counterpart, indicating that it is relatively insensitive to amorphization. Anatase was precipitated on the surfaces of all the amorphous pyrochlores. The superior dissolution behaviour of both crystalline $Gd_2Ti_2O_7$ and $Lu_2Ti_2O_7$ when compared to $Y_2Ti_2O_7$ indicates that despite their structural similarities, the manner in which Gd, Lu and Y are incorporated into the pyrochlore structure is significantly different. This deduction was supported by Raman spectroscopy, which indicated that crystalline $Y_2Ti_2O_7$ contained a significantly more disordered A-site coordination environment than either crystalline $Gd_2Ti_2O_7$ or $Lu_2Ti_2O_7$.

Acknowledgements

We wish to thank S. Moricca and N. Webb for assistance with the hot-isostatic pressing and E. Vance for helpful discussions.

References

[1] W.J. Weber, J.W. Wald, Hj. Matzke, Mater. Lett. 3 (1985) 173.
[2] W.J. Weber, J.W. Wald, Hj. Matzke, J. Nucl. Mater. 138 (1986) 196.
[3] J.W. Wald, W.J. Weber, in: G.G. Wicks, W.A. Ross (Eds.), Advances in Ceramics, Nuclear Waste Management, vol. 8, American Ceramic Society, Columbus, OH, 1984, p. 71.
[4] W.J. Weber, N.J. Hess, G.D. Maupin, Nucl. Instrum. and Meth. B 65 (1992) 102.
[5] W.J. Weber, N.J. Hess, Nucl. Instrum. and Meth. B 80&81 (1993) 1245.
[6] S.X. Wang, L.M. Wang, R.C. Ewing, K.V. Govindan Kutty, Mater. Res. Soc. Symp. Proc. 540 (1999) 355.
[7] S.X. Wang, B.D. Begg, L.M. Wang, R.C. Ewing, W.J. Weber, K.V. Govindan Kutty, J. Mater. Res. 14 (1999) 4470.
[8] C.W. Allen, L.L. Funk, E.A. Ryan, S.T. Ockers, Nucl. Instrum. and Meth. B 40–41 (1989) 553.
[9] S. Thevuthasan, C.H.F. Peden, M.H. Engelhard, D.R. Baer, G.S. Herman, W. Jiang, Y. Liang, W.J. Weber, Nucl. Instrum. and Meth. A 420 (1999) 81.
[10] S.X. Wang, L.M. Wang, R.C. Ewing, G.S. Was, G.R. Lumpkin, Nucl. Instrum. and Meth. B 148 (1999) 704.
[11] W.J. Weber, Nucl. Instrum. and Meth. B 166&167 (2000) 98.
[12] W.J. Weber, R.C. Ewing, Science 289 (2000) 2051.
[13] B.D. Cullity, Elements of X-ray Diffraction, 2nd Ed., Addison-Wesley, Reading, MA, 1978.
[14] J.W. Wald, W.J. Weber, in: G.G. Wicks, W.A. Ross (Eds.), Nuclear Waste Management, Advance in Ceramics, vol. 8, Amer. Ceram. Soc., Columbus, OH, 1984, p. 71.
[15] M. Oueslati, M. Balkanski, P.K. Moon, H.L. Tuller, Mater. Res. Soc. Symp. Proc. 135 (1989) 199.